LANGMUIR

pubs.acs.org/Langmuir Article

Multiple Linear Regression Modeling of Nanosphere Self-Assembly via Spin Coating

Talha Razaulla, Michael Bekeris, Haidong Feng, Michael Beeman, Ugochukwu Nze, and Roseanne Warren*



Cite This: Langmuir 2021, 37, 12419-12428



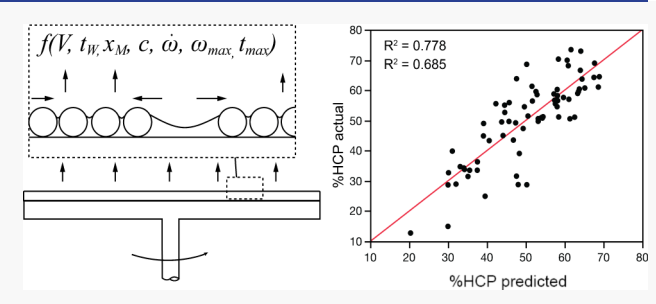
ACCESS

III Metrics & More

Article Recommendations

Supporting Information

ABSTRACT: Nanosphere lithography employs single- or multilayer self-assembled nanospheres as a template for bottom-up nanoscale patterning. The ability to produce self-assembled nanospheres with minimal packing defects over large areas is critical to advancing applications of nanosphere lithography. Spin coating is a simple-to-execute, high-throughput method of nanosphere selfassembly. The wide range of possible process parameters for nanosphere spin coating, however—and the sensitivity of nanosphere self-assembly to these parameters—can lead to highly variable outcomes in nanosphere configuration by this method.



Finding the optimum process parameters for nanosphere spin coating remains challenging. This work adopts a design-of-experiments approach to investigate the effects of seven factors—nanosphere wt%, methanol/water ratio, solution volume, wetting time, spin time, maximum revolutions per minute, and ramp rate—on two response variables—percentage hexagonal close packing and macroscale coverage of nanospheres. Single-response and multiple-response linear regression models identify main and two-way interaction effects of statistical significance to the outcomes of both response variables and enable prediction of optimized settings. The results indicate a tradeoff between the high ramp rates required for large macroscale coverage and the need to minimize high shear forces and evaporation rates to ensure that nanospheres properly self-assemble into hexagonally packed arrays.

■ INTRODUCTION

Nanosphere lithography (NSL), also known as colloidal lithography, is a bottom-up fabrication approach that uses a single- or multilayer stacked nanosphere array as a template for nanoscale patterning. Compared to top-down lithography approaches, NSL is a low-cost, simple fabrication technique that can achieve sub-100 nm feature sizes without the need for complex protocols or expensive equipment. NSL has been demonstrated as a useful nanoscale patterning approach in many applications, including surface-enhanced Raman scattering, applications, including serious, find an orange of nanogap electrodes, gas sensing, sens antireflection coatings for solar cells,^{6,7} photoluminescence, optical fiber tip nanoprobes, ¹⁰ plasmonic electrodes, ^{11,12} and superhydrophobic surfaces. 13 Since the first demonstration of equilateral triangle and dot array patterns by Hulteen and Van Duyne, NSL has been used to achieve a wide range of pattern geometries, such as bimetallic "cup-like structures", rods, and rings produced by shadow (or "angle-resolved") NSL, 14-16 core-shell-structured nanohole arrays in conjunction with triangular nanopillars,8 and nanobridged NSL featuring connective linkages between nanospheres. 17 To further demonstrate its versatility, NSL has been used for patterning a wide range of materials, including metals, insulators, and organic semiconductors. 18,19

Numerous methods may be used to induce nanosphere self-assembly into single and multilayer hexagonal close-packed (HCP) configurations required for subsequent patterning and templating. Focusing on single-layer NSL, traditional methods of self-assembly include convective self-assembly and shear-induced ordering *via* spin coating, 20-22 solvent evaporation, 23 doctor-blade coating, 24,25 drop-casting, 26 and confined convective assembly. Alternative methods based on electrophoretic or electrostatic self-assembly, 28-30 capillary-based self-assembly on patterned substrates, 31 and micropropulsive injection 32,33 have also been explored. Of these methods, spin coating remains one of the most versatile and widely implemented approaches for preparing single-layer HCP nanosphere arrays. The primary advantages of spin coating are the high-throughput 34 and large-area processing capabilities, including wafer-scale substrates (4 in silicon). Spin coating is also compatible with standard methods of semiconductor manufacturing and can be implemented in

Received: August 3, 2021
Revised: September 28, 2021
Published: October 13, 2021





combined top-down and bottom-up fabrication protocols.³⁹ Finally, spin coating is particularly well-suited for self-assembly of large diameter nanospheres, a process that is especially challenging with other methods such as gravitational sedimentation.²²

Despite the advantages of spin coating for NSL, there are few systematic studies exploring the effects of spin coating parameters on the self-assembly of single-layer nanosphere arrays. Colson et al. used principal component analysis to study the effect of ramp rate and revolutions per minute (rpm) on nanosphere monolayer coverage and percent HCP (%HCP).40 While the study is one of the first to combine an experimental design approach with quantitative evaluation of nanosphere film quality, the experiment did not consider the effects of nanosphere concentration, solvent properties, or solution volume on the resulting monolayers. Jiang et al. explored the effect of spin speed and spin time on the self-assembly of multilayer colloidal crystals by spin coating.²² The authors determined that multilayer thickness depends on the inverse of spin speed and the inverse square root of spin time. The thickness of the resulting films varied from two-layer colloidal crystals to 25 μ m films comprising several tens of stacked nanosphere layers. Khanna et al. studied the effect of various process parameters (including concentration of silica nanospheres, surface treatment, spin rate, and spin time) on the resulting nanosphere surface coverage.⁴¹ While the report is useful for confirming the effects of these parameters independently, no interaction effects were considered and the relative importance of each parameter was not determined. In addition, the study used a qualitative approach for comparing scanning electron microscopy (SEM) images, without quantifying response variables such as monolayer coverage or %HCP. Mathematical models of nanosphere selfassembly driven by capillary forces provide a theoretical basis for understand convective or shear-induced self-assembly processes; 42,43 however, these models cannot account for stochastic effects resulting from small variations in selfassembly conditions. In addition, highly complex self-assembly processes with one or more spin coating stages are typically impractical to model. 44 With a wide range of NSL spin coating parameters reported in the literature, a detailed experimental study of the effect of process parameters and their interaction effects is needed to improve the quality and reproducibility of single-layer nanosphere self-assembly by spin coating.

This work presents a design of experiments (DOE) multiple linear regression modeling approach to understand the effects of spin coating parameters on single-layer nanosphere selfassembly. A DOE screening study was conducted with seven factors: (1) nanosphere concentration ("NS wt%"), (2) methanol/water ratio ("MW ratio"), (3) solution volume ("volume"), (4) wetting time, (5) ramp rate, (6) maximum spin speed ("max rpm"), and (7) time at maximum rpm ("spin time"). Two response variables were considered: (1) %HCP and (2) fraction of the substrate coated with nanosphere solution ("macroscale coverage"). DOE screening studies are useful for identifying main and interaction effects of statistical significance to the response variables using a minimum number of experiments. In this work, 72 spin coating trials were run in a custom DOE study with the ability to identify two-factor interactions as well as quadratic effects. A test matrix was set up using JMP Pro statistical software with factors set at minimum, maximum, and midpoint levels (Table S1). Macroscale coverage was estimated from image analysis of digital

photographs (Figure S1). Within regions of nanosphere coverage, %HCP was quantified using SEM images. The SEM images were processed using an image analysis program that counts numbers of "total" and "loose" spheres in an image, with "loose" spheres defined as any nanosphere not in perfect HCP configuration. 45 %HCP values were averaged over 2-5 images per sample. The results of the 72 experimental conditions (Table S2) were fit to linear regression models that predict macroscale coverage and %HCP based on process parameter settings. Linear regression models were first fit to the response variables independently (single-response models). A combined model utilizing a common set of parameters was then fit to the two response variables simultaneously (multipleresponse model). The results provide insights into the factors that most significantly affect nanosphere self-assembly by spin coating. Additionally, the models can be used to determine optimal settings for process parameters to maximize %HCP, macroscale coverage, or both response variables simultane-

EXPERIMENTAL SECTION

Design of Experiments. JMP Pro statistical software was used to prepare the experimental matrix for the DOE. A customized response surface design with 72 experiments enabled modeling of two-factor interactions and quadratic effects. To reduce the likelihood of human error in conducting the DOE, the experiments were split into eight groups with each group having the same DOE setting for nanosphere (NS) wt%. Table S1 summarizes the groupings and the parameters used for each experiment.

Nanosphere Spin Coating. Polystyrene (PS) nanospheres were purchased from Bang Laboratories, Inc. (10 wt% solution, 390 nm diameter). All other materials were obtained from Millipore Sigma and used as received. PS nanosphere stock solution was sonicated for 10 min prior to all dilution steps. PS nanospheres were diluted to concentrations of 2, 4, and 6 wt% in a solution of type 1 deionized (DI) water with 1:400 (by volume) solution of methanol/Triton X-100 surfactant. Three different MW ratios were used: 0:1, 0.33:1, and 0.67:1 by volume. The PS nanosphere solutions were stored in the refrigerator until 1 h prior to use. Silicon wafers were coated with 20 nm SiO₂ by plasma-enhanced chemical vapor deposition (Oxford Plasmalab 80) to create a hydrophilic surface for nanosphere spin coating. The wafers were then diced into 20 mm × 20 mm chips using a Disco DAD641 dicing saw. A layer of protective photoresist was applied to the wafers prior to dicing. Following dicing, the chips were cleaned and the photoresist removed using an acetone bath with sonication for 5 min, followed by isopropyl alcohol rinse for 30 s, DI water rinse for 1 min, and drying under nitrogen. PS nanosphere solutions were sonicated for 5 min just prior to spin coating. The chips were loaded individually onto a CEE 100 spinner, and spin coating of nanosphere solutions was performed according to the parameters listed in Table S1 once the chips were centered. Nanosphere solutions were dispensed onto the chip while motionless and allowed to spread on the chip for the prescribed wetting time. All nanosphere solution and chip preparation steps, as well as spin coating, were completed in a Class 100/1000 clean room environment. The relative humidity in the clean room was 40% during the experiments.

Characterization and Image Analysis. All imaging of nanosphere spin coating was performed without modification of the chips. A digital photograph was taken of each chip post-spin coating, and a MATLAB image analysis program was used to determine the macroscale coverage of the PS nanosphere solution on each chip (Figure S1). SEM imaging was conducted using an FEI Helios Nanolab 650 Dual Beam FIB and field-emission SEM. A MATLAB image analysis program was used to determine %HCP from the SEM images. Two-to-five SEM images were taken per chip, and the % HCP values for each image were averaged to give the "%HCP"

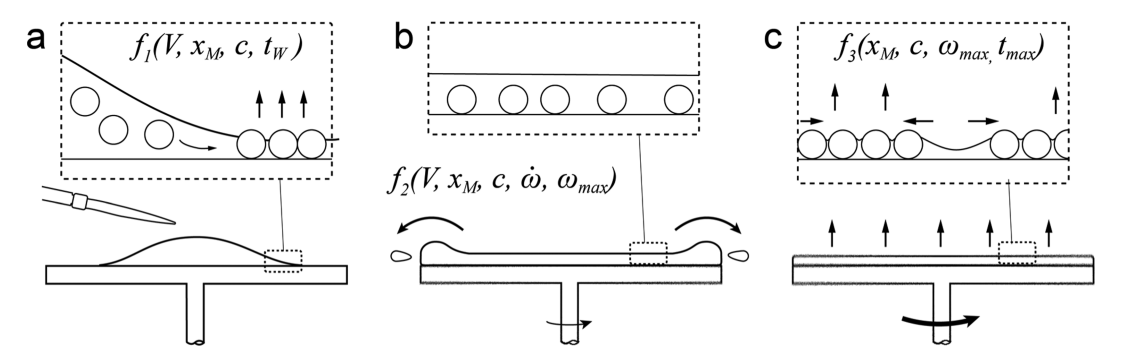


Figure 1. Conceptual illustration of nanosphere convective and shear-induced assembly during spin coating. (a) In phase 1 (static dispensing), some convective self-assembly occurs depending on the solution volume (V), methanol mole fraction $(x_{\rm M})$, nanosphere concentration (c), and wetting time $(t_{\rm W})$. (b) In phase 2 (ramp phase), excess solution is removed by centrifugal forces depending on V, $x_{\rm M}$, c, ramp rate $(\overline{\omega})$, and maximum spin speed $(\omega_{\rm max})$. (c) In phase 3 (maximum spin speed), nanosphere convective self-assembly occurs due to capillary forces between nanospheres arising from solution evaporation and horizontal sphere flux. These processes depend on $x_{\rm M}$, c, $\omega_{\rm max}$, and the time at maximum spin speed $(t_{\rm max})$.

response analyzed in the linear regression models. %HCP and macroscale coverage results for the 72 spin coating trials are provided in Table S2.

Linear Regression Modeling. Linear regression with two-way interactions was performed in IMP Pro using a standard least squares model. A backward selection technique was used for variable selection. First, a full two-way interaction model was fit. Terms were then removed one at a time starting with the highest p-value. The model was rerun after each parameter removal to check for reordering of factors. Backward selection continued until the R2 adjusted (R_{adi}^2) value was maximized. In the case of multiple response variables, the backward selection technique was adapted to eliminate the factor with the lowest average LogWorth across both response variables and no p-value < 0.2 in any response. Backward selection continued until the average $R_{\rm adj}^{\ \ 2}$ value for both response variables was maximized. If a main effect was present in an interaction or quadratic effect of significance, that main effect was not eliminated from the model following the principle of effect heredity. All final linear regression models were checked using residual-by-row, residualby-predicted, normal quantile, and actual-by-predicted diagnostic plots (Figures S2-S4). Variable importance was calculated in JMP Pro using the independent uniform input assumption (Figure 7).

■ RESULTS AND DISCUSSION

Figure 1 provides a conceptual illustration of nanosphere convective self-assembly via spin coating. The process can be considered in three phases. In phase 1, a volume of nanosphere solution is deposited on the substrate (Figure 1a). This may occur with a stationary or slowly spinning substrate; in this work, we used static dispensing onto a stationary substrate. Some convective self-assembly of nanospheres occurs due to solvent evaporation, depending on the solution volume (V), solvent MW ratio $(x_{\rm M})$, NS wt% (c), and wetting time $(t_{\rm W})$. 31 In phase 2, the substrate undergoes ramping from stationary to maximum spin speed (Figure 1b). Excess solution is removed from the substrate, and the solution level decreases due to solvent evaporation. Phase 2 outcomes are affected by V, x_{M} , c_{s} and the ramp rate $(\overline{\omega})$ to max rpm (ω_{\max}) . In phase 3, the substrate is spinning at maximum rpm and the solvent level decreases below the height of the nanospheres (Figure 1c). A meniscus forms between nanospheres that induces capillary self-assembly with solvent evaporation. Shear forces further induce movement of the colloidal crystal, depending on the solution viscosity (a function of x_{M}), c, ω_{max} and spin time $(t_{\text{max}})^{42}$. This work considers a nanosphere spin coating process consisting of one ramp stage and one constant rpm

stage to minimize the number of DOE factors. Colson et al. considered a nanosphere spin coating process employing two ramp phases and three rpm levels. ⁴⁰ Their results indicate that the first ramp rate and first rpm are the most important variables affecting the resulting nanosphere self-assembly when compared with subsequent ramp/rpm levels.

Table 1 summarizes the DOE parameter ranges used in this study. Ranges were determined based on maximum and

Table 1. DOE Factor Ranges and Predicted Optimum Settings Based on Single- and Multiple-Response Linear Regression Modeling

			single response optimum		
factor	min	max	%НСР	macroscale coverage	multiple response optimum ^a
NS wt%	2	6	4	2	6
MW ratio (v/v)	0:1	0.67:1	0.67:1	0.67:1	0:1
$\operatorname{volume}_{\left(\mu L\right)^b}$	20	80	20	80	80
wetting time (s)	20	60	20	40	20
spin time (s)	2	30	2	20	21
max rpm	200	5000	200	1770	200
ramp rate (rpm/s)	200	1000	200	1000	1000

"Results depend on the relative importance of response variables and desirability functions, which can be set in JMP. Table 1 results assume equal response importance, with desirability functions shown in Figure 8a. "Equivalent to $5-20~\mu\text{L/cm}^2$.

minimum values commonly reported in the literature (see Table S3 for detailed references and commonly reported values for each factor). We note that changing the MW ratio of the solvent changes three properties known to affect nanosphere self-assembly: surface tension, vapor pressure, and kinematic viscosity. Figure 2 plots the effects of the MW ratio on each of these variables based on experimental results reported in the literature for methanol—water solutions without nanospheres. While the presence of nanospheres at 2–6 wt% will affect solution values of surface tension, vapor pressure, and kinematic viscosity, in general, we can expect increasing the MW ratio of the nanosphere solution to correlate with

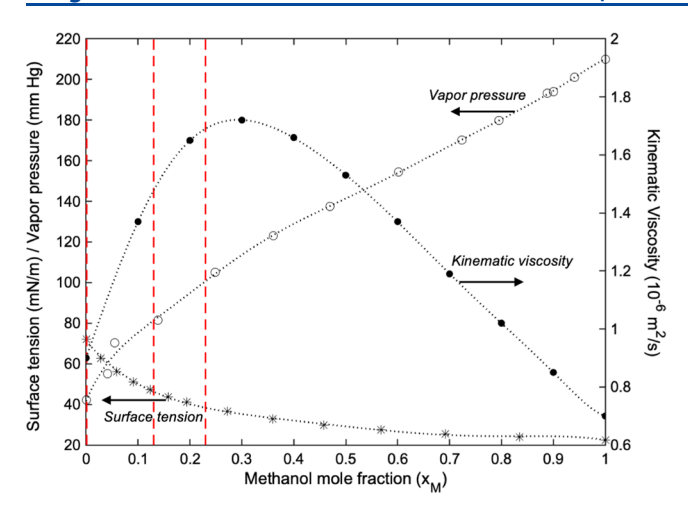


Figure 2. Effect of the MW ratio on surface tension, ⁴⁶ vapor pressure, ⁴⁷ and kinematic viscosity. ⁴⁸ The MW ratios used in this study are indicated as dashed red lines corresponding to methanol mole fractions of 0, 0.13 (0.33:1 MW ratio), and 0.23 (0.67:1 MW ratio). Plotted values of surface tension, vapor pressure, and viscosity do not consider the presence of nanospheres or Triton-X surfactant.

decreasing surface tension and increasing vapor pressure. Kinematic viscosity increases with the MW ratio for mole fractions up to 0.3, followed by a decreasing trend. In the range of methanol mole fractions considered in this work (0–0.23), kinematic viscosity consistently increases with the MW ratio. Many other solvents besides methanol—water have been used for nanosphere self-assembly via spin coating, including most commonly N_1N -dimethyl-formamide 35,41 and ethanol—water. $^{49-51}$ Methanol—water was used in this work as it is commonly employed in many nanosphere spin coating studies. $^{8,40,52-54}$ A nanosphere diameter of 390 nm was chosen as it is within the range of 150-1000 nm typically reported for nanosphere spin-coating processes.

Figure 3a provides results for the single-response linear regression model for %HCP. A maximum $R_{\rm adj}^2$ value of 0.685 was achieved by backward selection of parameters. The resulting model contains 21 parameters and has an R^2 value of 0.778. Table S4 provides a list of main effects and two-way interactions included in the model and their p-values. Five parameters in the model are statistically significant (p-value < 0.01): (1) max rpm (main effect), (2) MW ratio (main effect), (3) ramp rate × spin time (interaction effect), (4) MW ratio × max rpm (interaction effect), and (5) MW ratio × volume

(interaction effect). Diagnostic plots for the linear regression model—including residual-by-row, residual-by-predicted, and normal quantile—are provided in Figure S2. The actual-bypredicted plot (Figure 3a) shows the model fit and range of values covered by the experimental data (\sim 12% HCP to \sim 75% HCP, with a mean of 51%). SEM images from data points with high and low %HCP are provided in Figure 3b,c, respectively, illustrating the contrast between nanosphere self-assembly at the extremes of the linear regression model. We note that the maximum value of %HCP achieved in the current data set of 72 experiments is less than 80%, and may not meet the requirements for nanosphere ordering required for some applications of NSL. As a screening study, the DOE conducted in this work is able to identify main and interaction effects of importance to the response variables. Future DOE studies focused on optimization may then be implemented following the screening study to achieve higher values of the response variables.

Figure 4a contains profile plots of %HCP as a function of the seven experimental factors and a desirability plot indicating maximum %HCP as the preferred response setting. The maximum %HCP predicted by the model with the current data set is 80.7%. This maximum is achieved at intermediate NS wt % (4%), maximum MW ratio (0.67:1), and minimum settings of max rpm (200 rpm), volume (20 μ L), spin time (2 s), ramp rate (200 rpm/s), and wetting time (20 s) (Figure 4a, Table 1). The combination of the minimum final rpm and minimum ramp rate likely reflects improved nanosphere self-assembly resulting from lower shear forces and reduced solvent evaporation rates. This has been demonstrated experimentally by Ogi et al. through varied parameter settings, 55 by Toolan et al. using *in situ* stroboscopic studies,⁵⁶ and by Reyes and Duda through Monte Carlo simulations.⁵⁷ Principal component analysis results of Colson et al. also suggest an inverse relationship between %HCP and the ramp rate for single-layer nanosphere self-assembly.⁴⁰ The high MW ratio which results in higher vapor pressure indicates preference for faster liquid removal through evaporation when operating at minimum rpm and ramp rate.

Figure 4b provides interaction plots for the three statistically significant interactions, with all other factors at the optimized settings indicated in Figure 4a. Interaction effects are inherently more complex to interpret than main effects; however, some theories may be posited from the trends observed in Figure 4b. First, the model suggests that the MW ratio has little effect on %HCP at low rpm, while higher MW

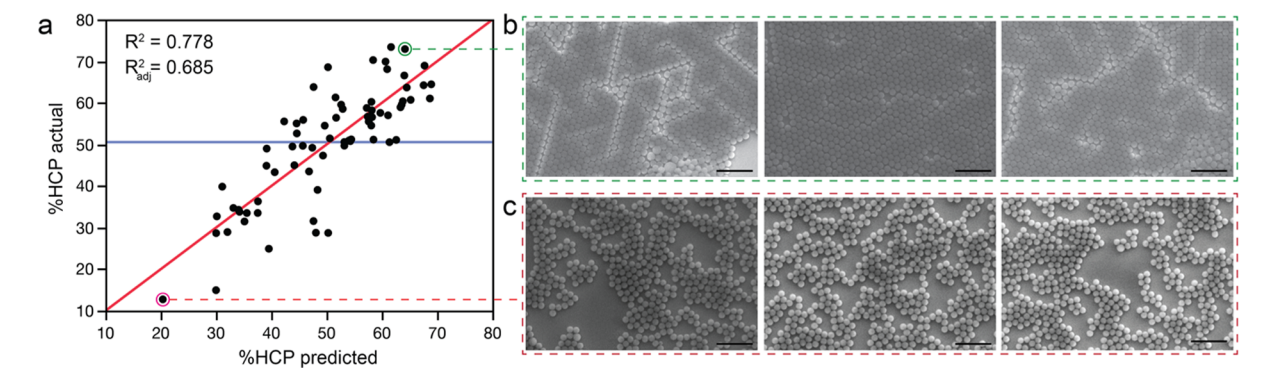


Figure 3. Single-response linear regression model results for %HCP. (a) Actual-by-predicted plot including R^2 and $R_{\rm adj}^2$ values. (b,c) SEM images associated with high (b) and low (c) values of %HCP. Scale bar: 2 μ m.

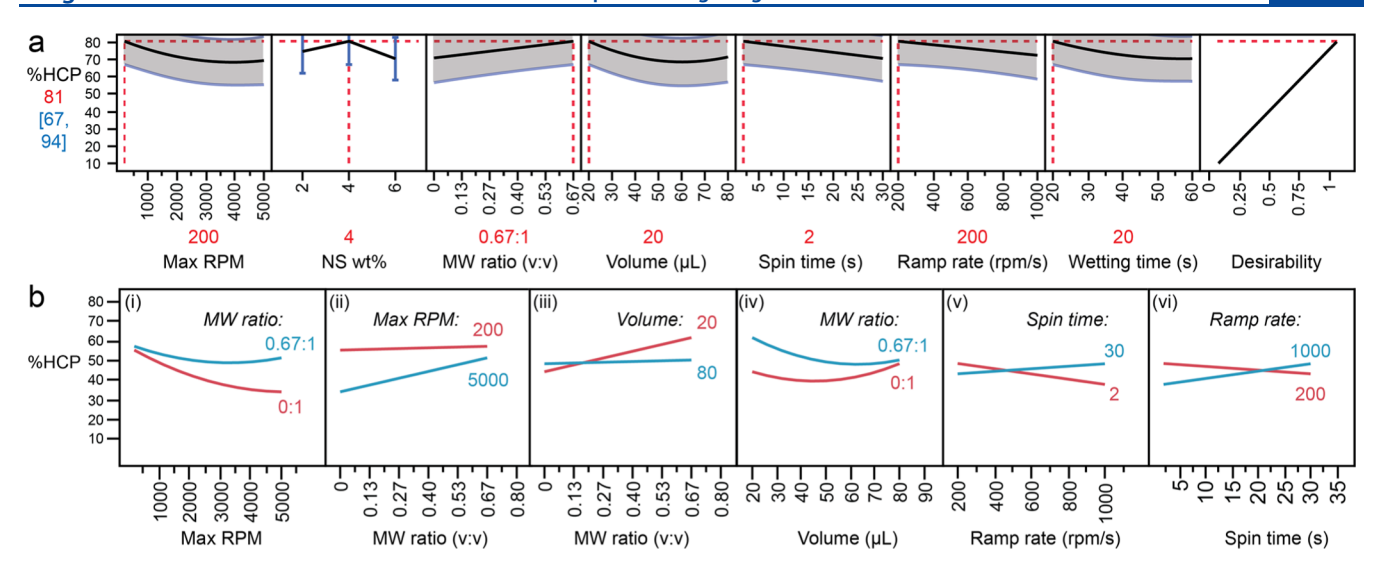


Figure 4. (a) Prediction profile plots showing the effect of each factor on %HCP with 95% confidence intervals shown in blue/gray. Red dotted lines and specified values indicate factor settings that maximize %HCP according to the desirability plot shown. (b) Interaction profile plots showing the effect of each factor on %HCP at maximum and minimum settings of a second factor. All other factors are set to the optimized values indicated in (a).

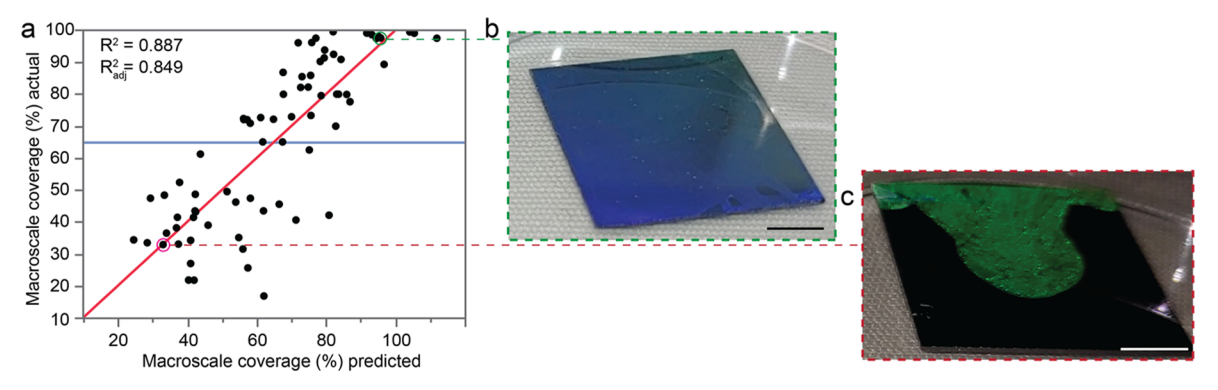


Figure 5. Single-response linear regression model results for macroscale coverage. (a) Actual-by-predicted plot including R^2 and R_{adj}^2 values. (b,c) Digital photographs associated with high (b) and low (c) values of macroscale coverage. Scale bar: 5 mm.

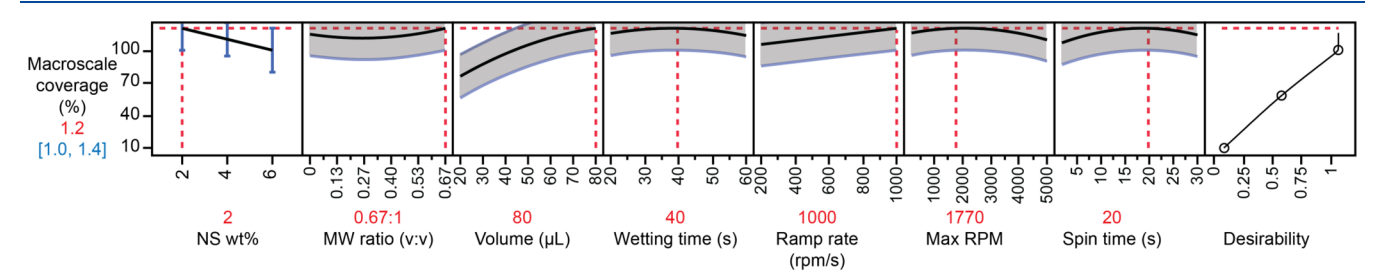


Figure 6. Prediction profile plots showing the effect of each factor on macroscale coverage with 95% confidence intervals shown in blue/gray. Red dotted lines and specified values indicate factor settings that maximize macroscale coverage according to the desirability plot shown.

ratios are necessary to achieve good %HCP at high rpm (Figure 4b(ii)). One possible explanation of this trend is in terms of solution viscosity. In spin coating of polymer films, higher solution viscosity is required to achieve comparable film thicknesses when the max rpm increases. Likewise higher kinematic viscosities associated with higher MW ratios (Figure 2) may be required to maintain minimum solvent thicknesses for capillary-induced self-assembly of nanospheres at high rpm (Figure 1c). The interaction of volume and the MW ratio indicates that the MW ratio does not greatly affect %HCP at high solution volumes (80 μ L), while a higher MW ratio is necessary for lower volumes (20 μ L) (Figure 4b(iii)). The

minimal change in %HCP with volume at a low MW ratio (Figure 4b(iv)) is similar to the case of polymer film spin coating, where film thickness is roughly constant as a function of dispense volume for a given solution viscosity. Figure 4b(v,vi) plots interaction effects of spin time and the ramp rate. At low spin times (2 s), the benefit of the lower ramp rate is consistent with the findings of Colson et al., where lower accelerations produced higher %HCP⁴⁰ (Figure 4b(v)). At higher spin time (30 s), the model indicates a slight increase in %HCP with increasing ramp rate. The mild dependence of % HCP on the ramp rate at high spin times may be similar to

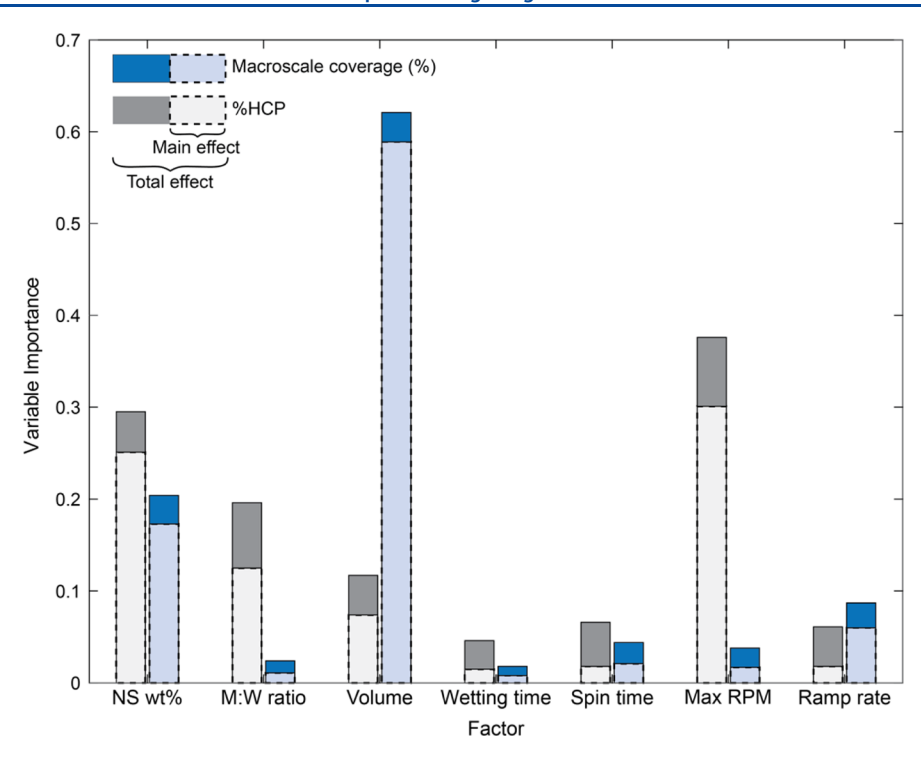


Figure 7. Variable importance plotted for each factor for %HCP and macroscale coverage response variables. The full bar length is indicative of the total effect importance; main effect importance is overlayed with dashed outline.

observations from polymer spin coating, where film thickness is, in general, independent of the ramp rate.⁴⁴

Figure 5 provides the single-response linear regression model results for macroscale coverage. Additional diagnostic plots are provided in Figure S3. A list of main effects and interactions included in the model is provided in Table S5, including p-values for each parameter. A maximum $R_{\rm adi}^2$ value of 0.849 ($R^2 = 0.887$) was achieved with 18 parameters included in the model. Of these, three are statistically significant: (1) volume (main effect), (2) ramp rate (main effect), and (3) spin time × spin time (quadratic effect). Differences in macroscale coverage of the nanosphere solution post-spin coating can be seen upon comparing Figure 5b (high coverage) and Figure 5c (low coverage). Recommended settings for experimental factors to maximize macroscale coverage of nanosphere solution on the substrate are: maximum pipette volume (80 μ L), ramp rate (1000 rpm/s), and MW ratio (0.67:1); minimum NS wt% (2 wt%); and intermediate values for wetting time (40 s), final rpm (1770 rpm), and spin time (20 s) (Figure 6). The results are consistent with the basic physics of spin coating, with a high ramp rate and high solution volume promoting effective spreading of the nanosphere solution during the acceleration phase (Figure 1b). We note that the linear regression model allows for surface coverage predictions exceeding 100%. Any macroscale coverage ≥100% is interpreted as full substrate coverage, with desirability for macroscale coverage set at "1" for any value $\geq 100\%$ (Figure 6). No significant interaction effects are included in the macroscale coverage linear regression model.

Figure 7 plots variable importance for the single-response models %HCP and macroscale coverage. Variable importance is divided into main effect importance and total effect importance (which includes main, interaction, and quadratic effects). Main effect importance is defined based on eq 1 as the

variance of the expected value of y when x_j is fixed (variance taken over the distribution of x_j), divided by the variance of y^{58}

main effect importance =
$$\frac{\operatorname{Var}(E(y|x_j))}{\operatorname{Var}(y)}$$
(1)

where y is the response variable %HCP or macroscale coverage, and x_1 , ..., x_7 are the DOE factors (Table 1). Total effect importance is defined similarly and includes all terms involving factor x_j . Full details on total effect importance estimation are provided in ref 58. As expected, macroscale coverage variable importance is dominated by volume as a main effect. %HCP variable importance is spread over more factors, including most notably maximum rpm, NS wt%, and MW ratio. Wetting time is of minimal importance for both response variables.

Single-response models provide insights into process parameters for optimizing %HCP and macroscale coverage independently and are consistent with existing knowledge of the combined shear and convective nanosphere self-assembly process, particularly, the results of Ogi et al.,55 Toolan et al.,5 Jiang et al.,³⁸ and Reyes and Duda.⁵⁷ In practice, it is desirable to achieve high levels of %HCP and macroscale coverage simultaneously. Comparing single-response model optimum values in Table 1, it can be seen that some adjustment of factor settings will be needed in order to effectively optimize both responses. A multiple-response model can provide insights into factor settings that provide high values of %HCP over large substrate areas. In the multiple-response model, the same set of parameters (including main, interaction, and quadratic effects) is used in the linear regression models for %HCP and macroscale coverage. Table S6 provides a list of the 21 parameters that provide concurrent maximum R_{adj}^2 values for linear regression models of the two response variables (Table S7 provides the complete list of factors for each model prior to the application of the backward selection technique).

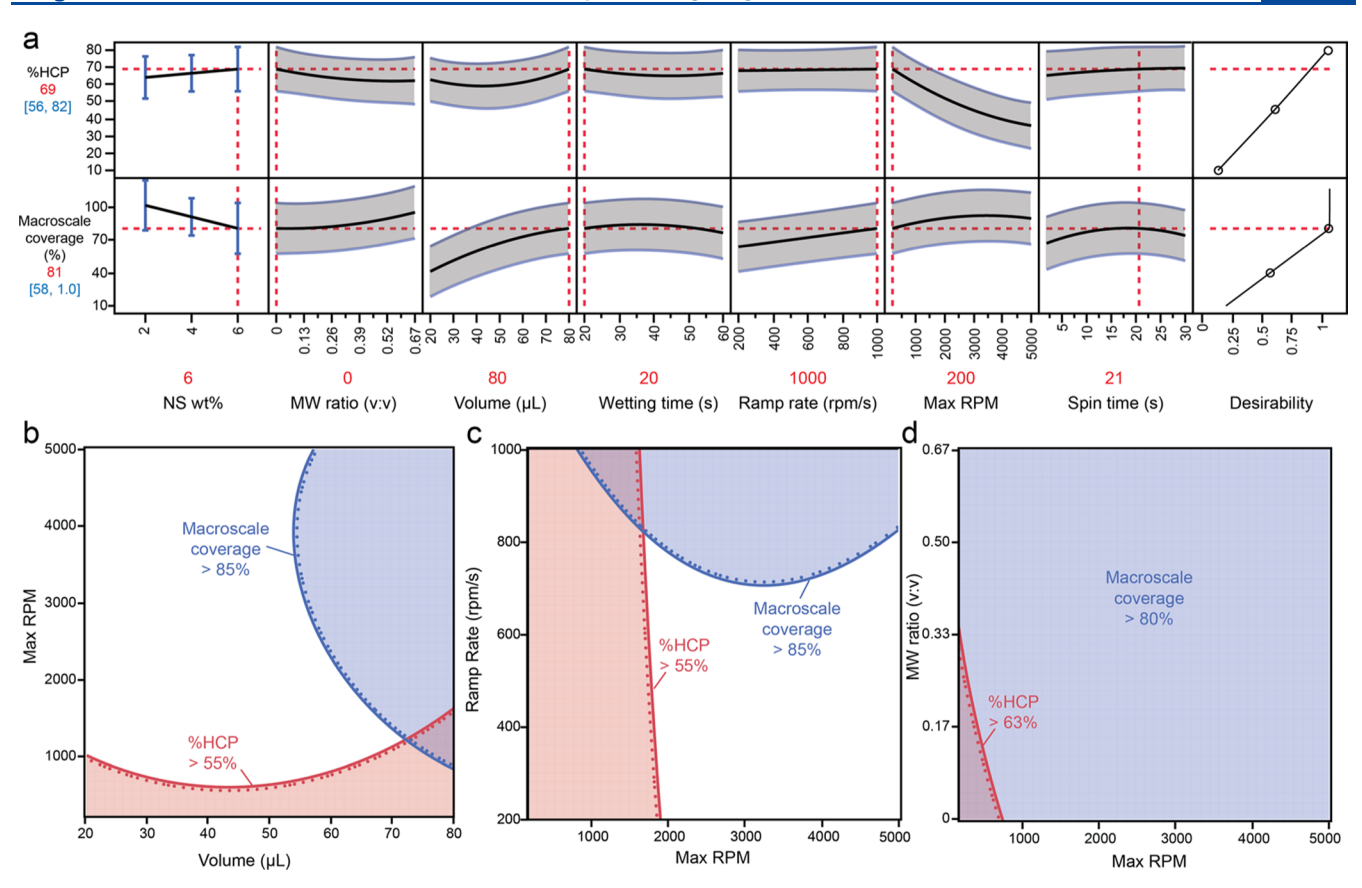


Figure 8. Multiple-response linear regression model results. (a) Prediction profile plots for %HCP (top row) and macroscale coverage (bottom row). Optimum factor settings are based on desirability curves shown (maximize %HCP; macroscale coverage ≥ 80%). (b−d) Contour profile plots showing parameter regions where the response variable prediction exceeds the specified value (red shaded areas for %HCP; blue shaded areas for macroscale coverage). Contour profiles are provided for (b) max rpm vs volume, (c) ramp rate vs max rpm, and (d) MW ratio vs max rpm. All other factors are set to the values specified in (a).

Diagnostic plots for both models are given in Figure S4. An $R_{\rm adj}^2$ value of 0.672 was obtained for %HCP (corresponding to an R^2 value of 0.769), only slightly less than that of the single-response %HCP model (Figure 3). The macroscale-coverage multiple-response model attained an $R_{\rm adj}^2$ value of 0.843 (corresponding to an R^2 value of 0.889), comparable to the single-response model (Figure 5). Significant factors are similar for both response variables in the multiple-response models compared to the single-response models, although the total list of factors included in each model differs due to the joint backward selection approach.

Multiple-response prediction profile plots (Figure 8a) show optimized parameter settings corresponding to maximum desirability across both response variables. %HCP and macroscale coverage are set to equal importance in determining optimized parameter settings; different results may be obtained if one response is weighted more heavily than the other. A desirability of "1" is set for maximum %HCP and any macroscale coverage values exceeding 80% (Figure 8a, desirability plots). These conditions were chosen to ensure that %HCP did not suffer to obtain "perfect" macroscale coverage; in practical applications of nanosphere lithography, excellent self-assembly over most of the substrate is generally preferred. Table 1 compares optimized factor settings for the multiple-response model with those obtained for singleresponse models. Factors with statistical significance for a given response generally stayed at the values specified in that response's single-response model (e.g., volume and ramp rate

values are consistent with those of the macroscale-coverage single-response model; max rpm is consistent with the %HCP single-response model). The MW ratio, a factor of statistical significance for %HCP, did change from its single-response setting for %HCP; however, prediction profile plots in Figure 8a indicate a gradual slope for both response variables *versus* the MW ratio. Further explanation of this change may also be gained from contour profile plots, as described below.

Contour profile plots (Figure 8b-d) indicate regions of factor settings that achieve specified minimum desirability levels. The overlap of these regions provides insights into why certain combinations of optimal parameters exist in the multiple-response model. The contour plot of max rpm versus volume (Figure 8b) illustrates the tradeoff between good solution coverage achieved at high max rpm and the need to minimize rapid solvent evaporation or excessive shear forces that hinder nanosphere self-assembly into ordered HCP structures. A high solution volume at lower max rpm achieves a compromise. Figure 8c provides a contour plot of ramp rate versus max rpm. %HCP at the contour level indicated is more sensitive to max rpm compared to the ramp rate. This result is consistent with convective and shear-induced self-assembly occurring predominantly in phase 3 of the spin coating process (Figure 1c). In contrast, macroscale coverage is governed primarily by the ramp rate (phase 2 of the spin coating process; Figure 1b). A combined optimal region for both response variables exists at high ramp rates and low max rpm; this is in contrast to the %HCP single-response model in which a lower

ramp rate is selected (Table 1, Figure 4a). Finally, the contour plot of the MW ratio *versus* rpm in Figure 8d illustrates why a 0:1 MW ratio is used in the multiple-response model compared to the 0.67:1 ratio in both single-response models. Under the conditions of the optimized multiple-response model—including maximum NS wt% (6%) and maximum ramp rate (1000 rpm/s)—a low MW ratio is needed to achieve predicted %HCP values ≥63%. This is likely due to the need for reduced solvent vapor pressure (Figure 2) to lower the evaporation rate under high ramp rates with high NS concentrations. Meanwhile, the more lenient requirement of ≥80% macroscale coverage can be met at any MW ratio and max rpm combination, given the other parameter settings indicated in Figure 8a.

CONCLUSIONS

In conclusion, we present here the results of a 72-trial DOE for optimizing %HCP and macroscale coverage for nanosphere self-assembly *via* spin coating. The results agree well with current understanding of convective and shear-induced self-assembly, specifically the need for lower ramp rates and lower max rpm to achieve high %HCP. High macroscale coverage is achieved with higher ramp rates and greater solution volumes. Multiple-response linear regression modeling proves useful for selecting parameters that can produce combined high levels of %HCP and macroscale coverage. The strength of the DOE and regression modeling approach is apparent in the ability to set relative importance and desirability for multiple response variables, enabling process optimization tuned to specific applications requiring more uniform nanosphere packing or higher surface coverage.

While the current work provides a framework for understanding the relationship between the seven factors considered, future studies are needed to explore the effects of additional NSL spin coating parameters on the response variables. Substrate size is an important parameter for NSL applications. Future DOE studies are needed to examine how spin coating factors should scale with substrate size and if/how the observed trends in variable interactions and optimization vary for wafer-scale substrates of 4 in. diameter and larger. Wafer-scale uniformity of self-assembled nanospheres should also be considered in such studies. In addition, spin coating parameters could be correlated with specific types of defects observed in SEM images, such as vacancies, grain boundaries, and dislocations. The effect of nanosphere size, material, and surface coating, and the wettability/surface free energy of the substrate, are additional factors worthy of exploration in future DOE studies of nanosphere spin coating.

ASSOCIATED CONTENT

Supporting Information

The Supporting Information is available free of charge at https://pubs.acs.org/doi/10.1021/acs.langmuir.1c02057.

DOE test matrix parameters, macroscale, and %HCP image analysis results for the 72 spin coating trials, details on the macroscale coverage image analysis approach, a comparison of DOE factor ranges with literature values, diagnostic plots and effect summary tables for each of the linear regression models, nanosphere DOE, and linear regression model (PDF)

AUTHOR INFORMATION

Corresponding Author

Roseanne Warren — Department of Mechanical Engineering, University of Utah, Salt Lake City, Utah 84112, United States; orcid.org/0000-0002-0520-8906; Email: roseanne.warren@utah.edu

Authors

Talha Razaulla — Department of Mechanical Engineering, University of Utah, Salt Lake City, Utah 84112, United States

Michael Bekeris — Department of Mechanical Engineering, University of Utah, Salt Lake City, Utah 84112, United States

Haidong Feng – Department of Mechanical Engineering,
 University of Utah, Salt Lake City, Utah 84112, United
 States; Present Address: 16-436 Massachusetts Institute of
 Technology, 77 Massachusetts Ave, Cambridge, MA
 02139

Michael Beeman — Department of Mechanical Engineering, University of Utah, Salt Lake City, Utah 84112, United States

Ugochukwu Nze – Department of Mechanical Engineering, University of Utah, Salt Lake City, Utah 84112, United States

Complete contact information is available at: https://pubs.acs.org/10.1021/acs.langmuir.1c02057

Author Contributions

The manuscript was written through contributions of all authors. All authors have given approval to the final version of the manuscript.

Funding

National Science Foundation (NSF).

Notes

The authors declare no competing financial interest.

ACKNOWLEDGMENTS

The authors would like to thank the staff of the University of Utah Nanofab and Surface Analysis Lab for their assistance with the nanosphere spin coating and imaging experiments, especially Tony Olsen and Brian Baker. This work was supported by NSF award no. 1761273, and the University of Utah Undergraduate Research Opportunities Program. This work made use of University of Utah USTAR shared facilities supported, in part, by the MRSEC Program of the NSF under award no. DMR-1121252.

ABBREVIATIONS

DOE, design of experiments; HCP, hexagonal close-packed; MW, methanol/water; NS, nanosphere; NSL, nanosphere lithography; PS, polystyrene; SEM, scanning electron microscopy

■ REFERENCES

(1) Hulteen, J. C.; Van Duyne, R. P. Nanosphere lithography: A materials general fabrication process for periodic particle array surfaces. *J. Vac. Sci. Technol., A* **1995**, *13*, 1553–1558.

(2) Fang, X.; Zheng, C.; Yin, Z.; Wang, Z.; Wang, J.; Liu, J.; Luo, D.; Liu, Y. J. Hierarchically Ordered Silicon Metastructures from Improved Self-Assembly-Based Nanosphere Lithography. *ACS Appl. Mater. Interfaces* **2020**, *12*, 12345–12352.

- (3) Huang, J.; He, Z.; Liu, Y.; Liu, L.; He, X.; Wang, T.; Yi, Y.; Xie, C.; Du, K. Large surface-enhanced Raman scattering from nanoporous gold film over nanosphere. *Appl. Surf. Sci.* **2019**, 478, 793–801.
- (4) Ji, D.; Li, T.; Fuchs, H. Nanosphere lithography for sub-10-nm nanogap electrodes. *Adv. Electron. Mater.* **2017**, *3*, 1600348.
- (5) Gao, M.; Cho, M.; Han, H.-J.; Jung, Y. S.; Park, I. Palladium-Decorated Silicon Nanomesh Fabricated by Nanosphere Lithography for High Performance, Room Temperature Hydrogen Sensing. *Small* **2018**. *14*. 1703691.
- (6) Yoo, G. Y.; Nurrosyid, N.; Lee, S.; Jeong, Y.; Yoon, I.; Kim, C.; Kim, W.; Jang, S.-Y.; Do, Y. R. Newly Developed Broadband Antireflective Nanostructures by Coating a Low-Index MgF2 Film onto a SiO2 Moth-Eye Nanopattern. ACS Appl. Mater. Interfaces 2020, 12, 10626–10636.
- (7) Chang, Y.-C.; Pollard, M. E.; Payne, D. N. R.; Sprafke, A.; Pillai, S.; Bagnall, D. M. Large-Area Nanosphere Gratings for Light Trapping and Reduced Surface Losses in Thin Solar Cells. *IEEE J. Photovoltaics* **2019**, *9*, 1012–1019.
- (8) Chau, Y.-F. C.; Lin, C.-J.; Kao, T. S.; Wang, Y.-C.; Ming Lim, C.; Kumara, N. T. R. N.; Chiang, H.-P. Enhanced photoluminescence of DCJTB with ordered Ag-SiO2 core—shell nanostructures via nanosphere lithography. *Results Phys.* **2020**, *17*, 103168.
- (9) Yanome, K.; Kiba, T.; Masui, K.; Kawamura, M.; Abe, Y.; Kim, K. H.; Takase, M.; Takayama, J.; Murayama, A. Photoluminescence enhancement of tris(8-hydroxyquinolinato)aluminum thin film by plasmonic Ag nanotriangle array fabricated by nanosphere lithography. *Thin Solid Films* **2018**, *660*, 907–912.
- (10) Pisco, M.; Galeotti, F.; Quero, G.; Grisci, G.; Micco, A.; Mercaldo, L. V.; Veneri, P. D.; Cutolo, A.; Cusano, A. Nanosphere lithography for optical fiber tip nanoprobes. *Light Sci. Appl.* **2017**, *6*, No. e16229.
- (11) Tan, H.; Santbergen, R.; Smets, A. H. M.; Zeman, M. Plasmonic Light Trapping in Thin-film Silicon Solar Cells with Improved Self-Assembled Silver Nanoparticles. *Nano Lett.* **2012**, *12*, 4070–4076
- (12) Jensen, T. R.; Malinsky, M. D.; Haynes, C. L.; Van Duyne, R. P. Nanosphere Lithography: Tunable Localized Surface Plasmon Resonance Spectra of Silver Nanoparticles. *J. Phys. Chem. B* **2000**, *104*, 10549–10556.
- (13) Shiu, J.-Y.; Kuo, C.-W.; Chen, P.; Mou, C.-Y. Fabrication of Tunable Superhydrophobic Surfaces by Nanosphere Lithography. *Chem. Mater.* **2004**, *16*, 561–564.
- (14) Kosiorek, A.; Kandulski, W.; Chudzinski, P.; Kempa, K.; Giersig, M. Shadow nanosphere lithography: simulation and experiment. *Nano Lett.* **2004**, *4*, 1359–1363.
- (15) Kosiorek, A.; Kandulski, W.; Glaczynska, H.; Giersig, M. Fabrication of nanoscale rings, dots, and rods by combining shadow nanosphere lithography and annealed polystyrene nanosphere masks. *Small* **2005**, *1*, 439–444.
- (16) Haynes, C. L.; McFarland, A. D.; Smith, M. T.; Hulteen, J. C.; Van Duyne, R. P. Angle-Resolved Nanosphere Lithography: Manipulation of Nanoparticle Size, Shape, and Interparticle Spacing. *J. Phys. Chem. B* **2002**, *106*, 1898–1902.
- (17) Luo, L.; Akinoglu, E. M.; Wu, L.; Dodge, T.; Wang, X.; Zhou, G.; Naughton, M. J.; Kempa, K.; Giersig, M. Nano-bridged nanosphere lithography. *Nanotechnology* **2020**, *31*, 245302.
- (18) Nguyen, V.-Q.; Schaming, D.; Martin, P.; Lacroix, J.-C. Nanostructured Mixed Layers of Organic Materials Obtained by Nanosphere Lithography and Electrochemical Reduction of Aryldiazonium Salts. *Langmuir* **2019**, *35*, 15071–15077.
- (19) Zhang, Q.; Li, K. H.; Choi, H. W. InGaN light-emitting diodes with indium-tin-oxide sub-micron lenses patterned by nanosphere lithography. *Appl. Phys. Lett.* **2012**, *100*, 061120.
- (20) Madaria, A. R.; Yao, M.; Chi, C.; Huang, N.; Lin, C.; Li, R.; Povinelli, M. L.; Dapkus, P. D.; Zhou, C. Toward optimized light utilization in nanowire arrays using scalable nanosphere lithography and selected area growth. *Nano Lett.* **2012**, *12*, 2839–2845.

- (21) Stelling, C.; Fossati, S.; Dostalek, J.; Retsch, M. Surface plasmon modes of nanomesh-on-mirror nanocavities prepared by nanosphere lithography. *Nanoscale* **2018**, *10*, 17983–17989.
- (22) Jiang, P.; McFarland, M. J. Large-scale fabrication of wafer-size colloidal crystals, macroporous polymers and nanocomposites by spin-coating. *J. Am. Chem. Soc.* **2004**, *126*, 13778–13786.
- (23) Denkov, N. D.; Velev, O. D.; Kralchevsky, P. A.; Ivanov, I. B.; Yoshimura, H.; Nagayama, K. Two-dimensional crystallization. *Nature* **1993**, *361*, 26.
- (24) Ormonde, A. D.; Hicks, E. C. M.; Castillo, J.; Van Duyne, R. P. Nanosphere Lithography: Fabrication of Large-Area Ag Nanoparticle Arrays by Convective Self-Assembly and Their Characterization by Scanning UV— Visible Extinction Spectroscopy. *Langmuir* **2004**, *20*, 6927—6931.
- (25) Prevo, B. G.; Velev, O. D. Controlled, rapid deposition of structured coatings from micro-and nanoparticle suspensions. *Langmuir* **2004**, *20*, 2099–2107.
- (26) Schmidt, J. P.; Cross, S. E.; Buratto, S. K. Surface-enhanced Raman scattering from ordered Ag nanocluster arrays. *J. Chem. Phys.* **2004**, *121*, 10657–10659.
- (27) Denomme, R. C.; Iyer, K.; Kreder, M.; Smith, B.; Nieva, P. M. Nanoparticle fabrication by geometrically confined nanosphere lithography. *J. Micro/Nanolithogr., MEMS, MOEMS* **2013**, *12*, 031106.
- (28) Deckman, H. W.; Dunsmuir, J. H. Natural lithography. *Appl. Phys. Lett.* **1982**, *41*, 377–379.
- (29) Hayward, R. C.; Saville, D. A.; Aksay, I. A. Electrophoretic assembly of colloidal crystals with optically tunable micropatterns. *Nature* **2000**, *404*, 56–59.
- (30) Giersig, M.; Mulvaney, P. Preparation of ordered colloid monolayers by electrophoretic deposition. *Langmuir* **1993**, *9*, 3408–3413.
- (31) Malaquin, L.; Kraus, T.; Schmid, H.; Delamarche, E.; Wolf, H. Controlled particle placement through convective and capillary assembly. *Langmuir* **2007**, *23*, 11513–11521.
- (32) Gao, P.; He, J.; Zhou, S.; Yang, X.; Li, S.; Sheng, J.; Wang, D.; Yu, T.; Ye, J.; Cui, Y. Large-area nanosphere self-assembly by a micropropulsive injection method for high throughput periodic surface nanotexturing. *Nano Lett.* **2015**, *15*, 4591–4598.
- (33) Cossio, G.; Yu, E. T. Zeta-Potential Dependent Self-Assembly For Very Large Area Nanosphere Lithography. *Nano Lett.* **2020**, 20, 5090–5096.
- (34) Liang, X.; Dong, R.; Ho, J. C. Self-assembly of colloidal spheres toward fabrication of hierarchical and periodic nanostructures for technological applications. *Adv. Mater. Technol* **2019**, *4*, 1800541.
- (35) Choi, J.-Y.; Alford, T. L.; Honsberg, C. B. Solvent-Controlled Spin-Coating Method for Large-Scale Area Deposition of Two-Dimensional Silica Nanosphere Assembled Layers. *Langmuir* **2014**, 30, 5732–5738.
- (36) Oh, J. R.; Moon, J. H.; Park, H. K.; Park, J. H.; Chung, H.; Jeong, J.; Kim, W.; Do, Y. R. Wafer-scale colloidal lithography based on self-assembly of polystyrene nanospheres and atomic layer deposition. *J. Mater. Chem.* **2010**, *20*, 5025–5029.
- (37) Jiang, P.; McFarland, M. J. Wafer-Scale Periodic Nanohole Arrays Templated from Two-Dimensional Nonclose-Packed Colloidal Crystals. *J. Am. Chem. Soc.* **2005**, *127*, 3710–3711.
- (38) Jiang, P.; Prasad, T.; McFarland, M. J.; Colvin, V. L. Two-dimensional nonclose-packed colloidal crystals formed by spincoating. *Appl. Phys. Lett.* **2006**, *89*, 011908.
- (39) Isaacoff, B. P.; Brown, K. A. Progress in Top-Down Control of Bottom-Up Assembly. *Nano Lett.* **2017**, *17*, 6508–6510.
- (40) Colson, P.; Cloots, R.; Henrist, C. Experimental design applied to spin coating of 2D colloidal crystal masks: a relevant method? *Langmuir* **2011**, 27, 12800–12806.
- (41) Khanna, S.; Utsav; Marathey, P.; Chaliyawala, H.; Rajaram, N.; Roy, D.; Banerjee, R.; Mukhopadhyay, I. Fabrication of long-ranged close-packed monolayer of silica nanospheres by spin coating. *Colloids Surf., A* **2018**, *553*, *520*–*527*.
- (42) Ackerson, B. J.; Clark, N. A. Shear-induced partial translational ordering of a colloidal solid. *Phys. Rev. A* **1984**, *30*, 906.

- (43) Kralchevsky, P. A.; Paunov, V. N.; Ivanov, I. B.; Nagayama, K. Capillary meniscus interaction between colloidal particles attached to a liquid—fluid interface. *J. Colloid Interface Sci.* **1992**, *151*, 79–94.
- (44) Daughton, W. J.; Givens, F. L. An Investigation of the Thickness Variation of Spun-on Thin Films Commonly Associated with the Semiconductor Industry. J. Electrochem. Soc. 1982, 129, 173.
- (45) Bekeris, M.; Truong, T.; Carron, S.; Karimi, Z.; Feng, H.; Nze, U.; Beeman, M.; Sochol, R. D.; Warren, R. Rapid Quantification of Nanosphere Lithography Packing Defects Using Scanning Electron Microscopy Edge Effects. *Phys. Status Solidi RRL* **2020**, *14*, 2000328.
- (46) Vazquez, G.; Alvarez, E.; Navaza, J. M. Surface tension of alcohol + water from 20 to 50 degree C. J. Chem. Eng. Data 1995, 40, 611–614.
- (47) McGlashan, M. L.; Williamson, A. G. Isothermal liquid-vapor equilibriums for system methanol-water. *J. Chem. Eng. Data* **1976**, 21, 196–199.
- (48) Mikhail, S. Z.; Kimel, W. R. Densities and Viscosities of Methanol-Water Mixtures. J. Chem. Eng. Data 1961, 6, 533-537.
- (49) Modrić-Šahbazović, A.; Novaković, M.; Schmidt, E.; Gazdić, I.; Pokić, V.; Peruško, D.; Bibić, N.; Ronning, C.; Rakočević, Z. Silicon nanostructuring by Ag ions implantation through nanosphere lithography mask. *Opt. Mater.* **2019**, *88*, 508–515.
- (50) Chen, J.; Dong, P.; Di, D.; Wang, C.; Wang, H.; Wang, J.; Wu, X. Controllable fabrication of 2D colloidal-crystal films with polystyrene nanospheres of various diameters by spin-coating. *Appl. Surf. Sci.* **2013**, 270, 6–15.
- (51) Zhang, C.; Cvetanovic, S.; Pearce, J. M. Fabricating ordered 2-D nano-structured arrays using nanosphere lithography. *MethodsX* **2017**, *4*, 229–242.
- (52) Sarkar, D. K.; Farzaneh, M. Fabrication of PECVD-grown fluorinated hydrocarbon nanoparticles and circular nanoring arrays using nanosphere lithography. *Appl. Surf. Sci.* **2008**, 254, 3758–3761.
- (53) Cheung, C. L.; Nikolić, R. J.; Reinhardt, C. E.; Wang, T. F. Fabrication of nanopillars by nanosphere lithography. *Nanotechnology* **2006**, *17*, 1339.
- (54) Kuo, C.-W.; Shiu, J.-Y.; Cho, Y.-H.; Chen, P. Fabrication of large-area periodic nanopillar arrays for nanoimprint lithography using polymer colloid masks. *Adv. Mater.* **2003**, *15*, 1065–1068.
- (55) Ogi, T.; Modesto-Lopez, L. B.; Iskandar, F.; Okuyama, K. Fabrication of a large area monolayer of silica particles on a sapphire substrate by a spin coating method. *Colloids Surf., A* **2007**, 297, 71–78.
- (56) Toolan, D. T. W.; Fujii, S.; Ebbens, S. J.; Nakamura, Y.; Howse, J. R. On the mechanisms of colloidal self-assembly during spin-coating. *Soft Matter* **2014**, *10*, 8804–8812.
- (57) Reyes, Y.; Duda, Y. Modeling of drying in films of colloidal particles. *Langmuir* **2005**, 21, 7057–7060.
- (58) Assess Variable Importance. https://www.jmp.com/support/help/en/16.0/index.shtml#page/jmp/assess-variable-importance-2.shtml#ww418531 (accessed 2021-07-26).